Fusion Engineering and Design 168 (2021) 112683

Contents lists available at ScienceDirect

Fusion Engineering and Design

journal homepage: www.elsevier.com/locate/fusengdes

Coils and power supplies design for the SMART tokamak

M. Agredano-Torres [*,a], J.L. Garcia-Sanchez [a], A. Mancini [a,b], S.J. Doyle [a,b], M. Garcia-Munoz [a,b], J. Ayllon-Guerola [a,c], M. Barragan-Villarejo [d], E. Viezzer [a,b], J. Segado-Fernandez [a], D. Lopez-Aires [b], J. Toledo-Garrido [b], P.F. Buxton [e], K.J. Chung [f], J. Garcia-Dominguez [a], L. Garcia-Franquelo [g], M.P. Gryaznevich [e], J. Hidalgo-Salaverri [a], Y.S. Hwang [f], J. I. Leon-Galvan [g], J. Maza-Ortega [d]

[a] Centro Nacional de Aceleradores (University of Seville, CSIC, J. de Andalucia), Seville, Spain
[b] Department of Atomic, Molecular and Nuclear Physics, University of Seville, Seville, Spain
[c] Department of Mechanical Engineering and Manufacturing, University of Seville, Seville, Spain
[d] Department of Electrical Engineering, University of Seville, Seville, Spain
[e] Tokamak Energy Ltd, 173 Brook Drive Milton Park Abingdon OX14 4SD, UK
[f] Department of Nuclear Engineering, Seoul National University, Seoul 151-742, South Korea
[g] Department of Electronic Engineering, University of Seville, Seville, Spain

ARTICLE INFO

Keywords:
Spherical tokamak
Magnet
Coil
Solenoid
Power supply
Supercapacitor

ABSTRACT

A new spherical tokamak, the SMall Aspect Ratio Tokamak (SMART), is currently being designed at the University of Seville. The goal of the machine is to achieve a toroidal field of 1 T, a plasma current of 500 kA and a pulse length of 500 ms for a plasma with a major radius of 0.4 m and minor radius of 0.25 m. This contribution presents the design of the coils and power supplies of the machine. The design foresees a central solenoid, 12 toroidal field coils and 8 poloidal field coils. Taking the current waveforms for these set of coils as starting point, each of them has been designed to withstand the Joule heating during the tokamak operation time. An analytical thermal model is employed to obtain the cross sections of each coil and, finally, their dimensions and parameters. The design of flexible and modular power supplies, based on IGBTs and supercapacitors, is presented. The topologies and control strategy of the power supplies are explained, together with a model in MATLAB Simulink to simulate the power supplies performance, proving their feasibility before the construction of the system.

1. Introduction

Spherical tokamaks are magnetic confinement fusion devices that are characterized by low aspect ratio plasmas [1–3]. Compared to standard tokamaks, they are more compact and enable a higher β, the ratio between the plasma and the magnetic pressure. Therefore, higher β means that, to obtain the same plasma pressure, a lower magnetic pressure is required, reducing the constructive and operational costs of the device.

A new spherical tokamak, named SMall Aspect Ratio Tokamak (SMART), is currently being designed by the Plasma Science and Fusion Technology group of the University of Seville [4,5]. The missions of this new device are to train the next generation of fusion physicists and engineers, study plasma confinement and stability, in positive vs. negative triangularity, and develop novel diagnostics, divertor configurations, plasma facing materials and plasma control techniques.

This paper aims to design a system able to generate suitable magnetic fields to create and confine the plasma inside SMART, i.e. the main coils of the tokamak and their power supplies.

Tokamaks have a pulsed operation with high current values. In most of present devices, the thermal behaviour of the coils do not reach stationary regime due to the short pulse length of the experiments. In particular for SMART, the pulse length is in the order of hundreds of milliseconds and is a key aspect for the coils design. Furthermore, the power supplies design is also challenging. Most relevant tokamaks use thyristor-based power supplies fed by flywheels or the grid [6]. The operation of a tokamak connected to the grid implies a perturbation for grid stability and, thus, storage systems as flywheels can avoid this effect. Nevertheless, following the present trend [7], the SMART supercapacitor-based power supplies have been designed with a modular and flexible concept, in order to improve the scalability of the

* Corresponding author.
E-mail address: managrtor@alum.us.es (M. Agredano-Torres).

https://doi.org/10.1016/j.fusengdes.2021.112683
Received 30 November 2020; Received in revised form 12 May 2021; Accepted 14 May 2021
Available online 1 June 2021

system while achieving a robust performance.

In Section 2, a description of SMART and its operational phases is presented, together with the position of the coils in the device and the general structure of the power supplies. The current waveforms, employed as starting point for the coils design, and the analytical thermal model, for obtaining their cross-sections, are presented in Section 3 to obtain the geometry and parameters of the coils. Finally, Section 4 presents the topology of the power supplies, the charge-balancing system and the control strategy. In addition, simulation results in MATLAB Simulink are presented in order to ensure the feasibility of the system before its construction and first operation.

2. SMART and its operational phases

SMART is a spherical tokamak with a plasma major radius r_p of 0.4 m and a minor radius a of 0.25 m, as shown in Fig. 1. The vessel has a height h_v of 1.6 m and radius r_v of 0.8 m. It is equipped with 12 Toroidal Field Coils (TFCs), a Central Solenoid (CS) and 4 pairs of Poloidal Field Coils (PFCs).

A simplified representation of the plasma shaping obtained in SMART, based on the plasma triangularity, is shown in Fig. 2. Regarding the connection of the coils, the 12 TFCs are connected in series and the Upper and lower PFCs are connected in pairs, except Div2 coils, which will have independent power supplies to control the vertical stability of the plasma. Therefore, seven power supplies are required, represented in Fig. 3.

The operation of the tokamak is divided in three phases defined by the plasma parameters in Table 1. The goal of phase 1 is to achieve first plasma and test the machine operation. This phase is planned to move rapidly to phase 2, which will demonstrate the capability of the device to obtain highly shaped plasmas. Therefore, the coils and the vessel of SMART are designed to assure a safe and conservative operation of the system for this phase. Regarding the power supplies, they have been designed to minimize present and future costs. Therefore, a modular structure allows an easy upgrade of the system for all phases. Finally, based on the expertise gained from the first two phases, an upgrade of SMART will achieve the highest and most relevant plasma parameters in phase 3.

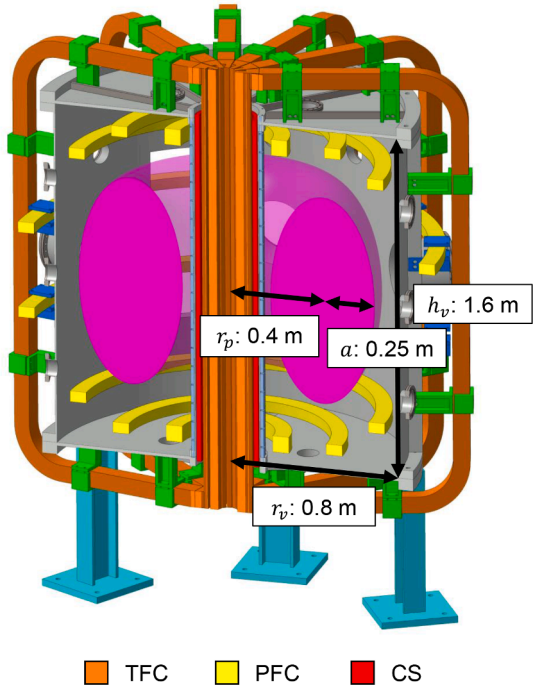

Fig. 1. SMART cross-section [5].

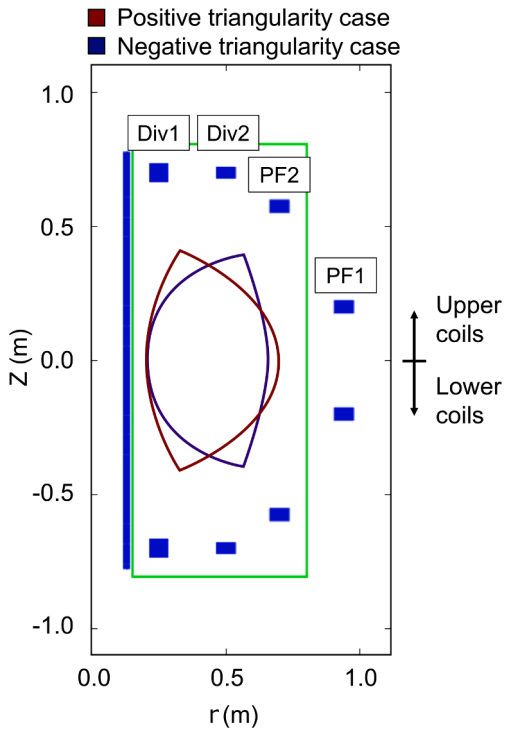

Fig. 2. SMART half cross-section. The designation of each pair of PFCs is shown, together with a simplified representation of the possible achievable triangularities in phase 2.

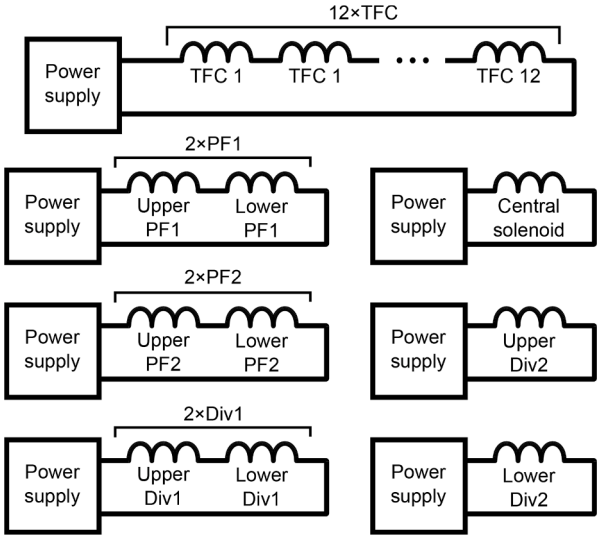

Fig. 3. Simplified representation of the 7 power supplies of SMART indicating the coils connections.

Table 1
SMART parameters for its three operational phases.

Parameters	Phase 1	Phase 2	Phase 3
Vessel size (m)	0.8 (r_v) × 1.6 (h_v)		
Aspect ratio	≤2 (r_p/a)		
Toroidal field (T)	0.1	0.3	1
Plasma current (kA)	30	100	500
Pulse length (ms)	20	100	500

3. Coils design

The coils have been designed to withstand the Joule heating with a low temperature increase in phase 2, maximum 5 °C. An analytical thermal model has been employed to obtain the required cross-section for each coil. Due to the required high currents, order of kiloamperes, and short operational pulses, hundreds of milliseconds, the thermal model employed for SMART has been adapted from the one used in international regulation to calculate the cross-sections required in case of overcurrent [8]. As the application of the model differs from its common use, it is explained in detail, justifying its utilisation for the design.

The energy E released by the current going through the coil comes from Joule effect and depends on the instant current in the conductor i and the resistance of the material R. The resistance is a function of the temperature T, temperature coefficient at 20 C α, resistivity at the same temperature ρ_{20}, length l and cross-section S of the conductor.

$$\frac{dE}{dt} = Ri^2 = \rho_{20}\frac{l}{S}(1+\alpha(T+20\ ^\circ\mathrm{C}))i^2 \tag{1}$$

The heat Q transferred to the copper depends on its volumetric heat capacity Q_c, length and cross-section of the conductor and derivative of the temperature.

$$\frac{dQ}{dt} = Q_c l S\frac{dT}{dt} \tag{2}$$

As the experiment is carried out in the order of milliseconds, an adiabatic heating is considered where all the energy released is employed to increase the temperature of the copper, without transmitting it to the exterior.

$$dE = dQ \rightarrow \rho_{20}\frac{l}{S}(1+\alpha(T+20\ ^\circ\mathrm{C}))i^2dt = Q_c l S dT \tag{3}$$

By reordering and integrating the equality, the cross-section of the conductor is obtained from the root mean square current I_{RMS}, the time of the operation t and a factor k that depends on the initial T_i and final temperature T_f and copper properties $Cu_{properties}$. These parameters are considered the operational limits of the coils.

$$\frac{1}{S^2}i^2dt = \frac{Q_c}{\rho_{20}}\frac{dT}{1+\alpha(T+20\ ^\circ\mathrm{C})} \tag{4}$$

$$\frac{t}{S^2}\left(\frac{1}{t}\int_0^t i^2dt\right) = \int_{T_i}^{T_f}\frac{Q_c}{\rho_{20}}\frac{dT}{1+\alpha(T+20\ ^\circ\mathrm{C})} \tag{5}$$

$$\frac{t}{S^2}I_{RMS}^2 = \frac{Q_c}{\rho_{20}\alpha}\ln\left(1+\frac{T_f-T_i}{\frac{1}{\alpha}-20\ ^\circ\mathrm{C}+T_i}\right) \tag{6}$$

$$S = \frac{\sqrt{t}}{k\left(T_i, T_f, Cu_{properties}\right)}I_{RMS} \tag{7}$$

$$k = \sqrt{\frac{Q_c}{\rho_{20}\alpha}\ln\left(1+\frac{T_f-T_i}{\frac{1}{\alpha}-20\ ^\circ\mathrm{C}+T_i}\right)} \tag{8}$$

Besides the thermal requirements, the operational limits are based on the required current waveforms. The TFCs need to provide a constant field during operation. Therefore, its current is obtained from Ampşre's Law and depends on the plasma major radius, the toroidal field B_t, the number of turns of the TFCs N_{TFC} and the magnetic permeability μ_0. The current waveform of the TFCs is shown in Fig. 4.

$$I_{TFC} = \frac{2\pi r_p B_t}{\mu_0 N_{TFC}} \tag{9}$$

The PFCs and CS current waveforms were obtained for different plasma triangularities using the free-boundary code Fiesta in [4]. The required current waveforms for the positive and negative triangularity cases in phase 2 are shown in Fig. 5. For the design, the current of the Upper and Lower Div2 have been considered equal.

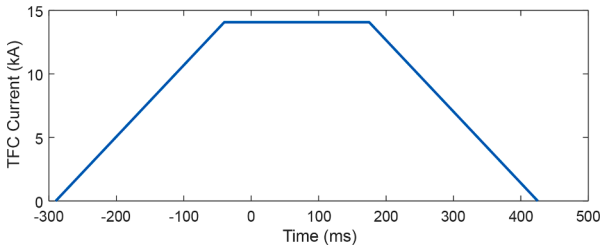

Fig. 4. TFCs current for phase 2, employed for the coils design. The origin of time coincide with the plasma breakdown, when the plasma current is induced by the CS.

For all the coils, the current is inversely proportional to the number of turns of the winding. The number of turns of each coil is presented in Table 2. As the TFCs have the greatest current level, the number of turns is maximized. The 12 coils in series, of 4 turns each, result in a total of 48 turns. Increasing further the number of turns would suppose an excessive increase in the complexity of the design. For the CS and PFCs, the current levels are kept below 5 kA. Due to the required flexibility for the PFCs, the same number of turns is selected for most of them, except Div1 coils, which requires a higher number of turns due to its current demands.

The central stack, where the TFCs inner legs and the CS are placed, is a key point of the design of a spherical tokamak. The characteristic shape of these devices causes a strict space constraint for placing the coils. Fig. 6 shows the layout of the TFCs inner legs in order to maximise the occupied space. Due to this space constraint in the central stack, the inner legs of the TFCs have a smaller cross-section than the outer limbs of the coils, 21.5 × 21.5 mm and 36 × 36 mm respectively. Therefore, the resistance and Joule losses are higher in the inner legs, leading to a higher temperature increase during operation. In order to compensate this effect, the free space between the inner legs is used to release the heat produced by the TFCs, by means of air cooling first, and water cooling for the second phase. Unlike the solid TFCs cross-sections, the CS and PFCs are equipped with hollow conductors, with a cross-section of 11 × 11 mm and 10 × 10 mm respectively and a hole diameter of 4 mm. Therefore, the CS and PFCs conductors are water cooled through

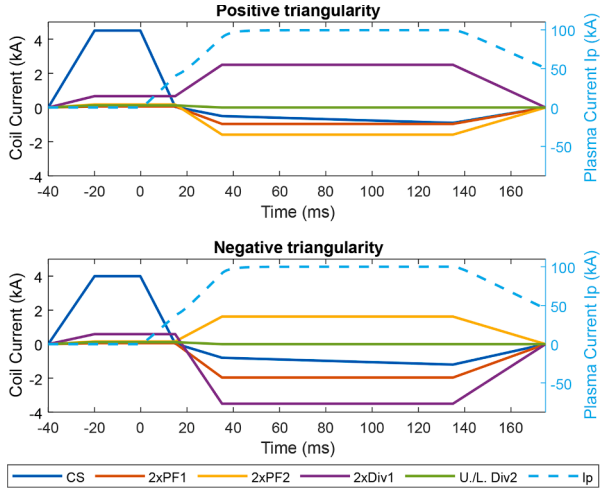

Fig. 5. PFCs and CS current waveforms and plasma current for the positive and negative triangularity cases for phase 2, employed for the coils design. The origin of time coincide with the plasma breakdown, when the plasma current is induced by the CS.

Table 2
Number of coils and turns.

Coils	No of coils	No of turns
TFCs	12	4
CS	1	230
PFCs	8	35 (U. and L. Div1) 23 (U. and L. Div2/PF1/PF2)

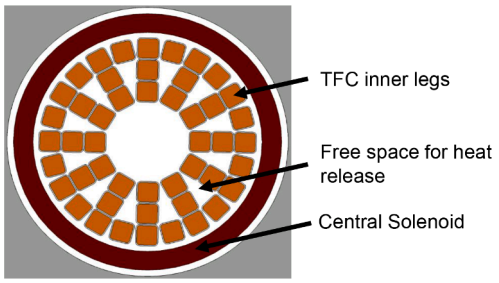

Fig. 6. Central stack cross-section.

this hole to reduce the cooling time between discharges and, in the case of the inner PFCs, to withstand the 200 C inside the vessel during baking. With the geometry and cross-sections of the coils, the load resistance and inductance for each power supply are obtained and presented in Table 3. For this analysis, it is not included resistance increase due to connection losses between coils and the power supply.

As there is a discrete number of TFCs, a spatial toroidal field ripple δ_r is produced. The ripple is calculated by the difference between the maximum field B_{max}, induced in front of a TFCs, and the minimum one B_{min}, in the middle of two coils, at a certain radius r of the vessel divided by the sum of these values [9].

$$\delta_r = \frac{B_{max} - B_{min}}{B_{max} + B_{min}} \tag{10}$$

Fig. 7 represents the toroidal field for a circular plasma with a mayor radius of 0.4, as r_p, and minor radius of 0.25, as a. The spatial ripple increases in the outer sides of the device due to a mayor distance between the TFCs. Thus, at the outer side of the plasma, the ripple is maximum and clearly observed. Fig. 8 shows the spatial ripple for each radius inside the vessel. Therefore, the maximum spatial ripple in the plasma is 0.4% in its outer side, at $r_p + a$ equal to 0.65 m, and the maximum ripple inside the vessel is 4%, at r_v equal to 0.8 m. Furthermore, the figure also include the toroidal field in theses two radius for 180° of SMART.

4. Power supplies design

The power supplies has been designed based on the same modular scheme to facilitate an easy upgrade for all phases. This is achieved by the parallelization of the system, enhancing the performance of the system by the utilization of interleaving and current-sharing control techniques. Furthermore, the power supplies have been simulated for the first operational phase, proving its feasibility.

Table 3
Load resistance and inductance of each power supply (without connection losses).

Coils	R(mΩ)	L(mH)
12 × TFCs	6	2.3
CS	30	2.4
2 × PF1	54	5.7
2 × PF2	40	4.0
2 × Div1	22	2.2
U. Div2	14	1.3
L. Div2	14	1.3

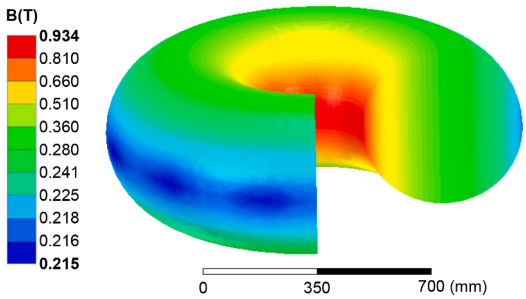

Fig. 7. Toroidal field for a circular plasma in phase 2 with a major radius of 0.4 m and minor radius of 0.25 m. The plasma has 0.3 T in the centre and a spatial ripple appears at the outer side.

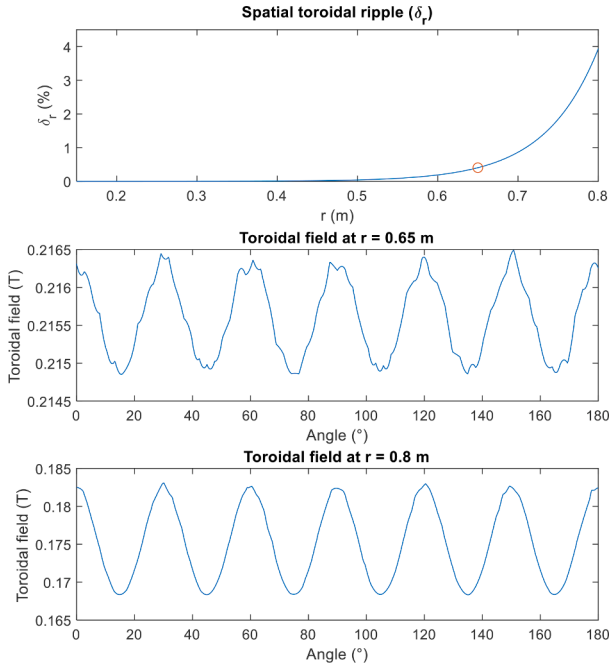

Fig. 8. Spatial toroidal field ripple inside the vessel and toroidal field for 180° of the SMART at a radius of 0.65 m and 0.8 m, where the spatial ripple is clearly visible.

For each coil of SMART, the power supply is based on Infineon IFF2400P17LE440988 Insulated Gate Bipolar Transistors (IGBTs) branches operated as H-bridge power converters and SAMWHA DM04860888W0101 supercapacitor modules (SCMs) connected in series to obtain supercapacitor banks (SCBs) with higher voltage levels. The specifications of the SCMs, including the Equivalent Series Resistance (ESR) for Direct Current (DC), are presented in Table 4. The maximum peak current can be withstand by the SCMs for 1 s, long enough for SMART operation. Furthermore, the 15 min considered

Table 4
SAMWHA SCM specifications.

Parameter	Value
Rated voltage (V)	48.6
Capacitance (F)	166.6
ESR DC (mΩ)	6
Maximum peak current (A)	2025
Maximum stored energy (MJ)	0.2
Dimensions (mm)	418 × 191 × 179

between experiments for charging the SCMs and planning of the next discharge guarantee the cooling down of the modules and rest of components.

The charging process of the SCB is done by an independent power supply that behaves as constant current source providing a current I_{Charge}. This power supply is connected for the charging process and disconnected during operation. With k from 1 to n SCMs in series, for each SCM k of the SCB the difference between the capacitances C_k and Equivalent Series Resistances (ESR_k), varies the charging speed of each of them and the voltages obtained u_{C_k}. The SCM already implement balancing systems for each of their supercapacitor cells. However, differences between SCMs still produce overvoltages during the charging process and reduce their lifetime. Therefore, a charge-balancing system, represented in Fig. 9, is implemented to solve this issue by the parallel connection of a switched resistance R_k. The resistance is designed to be lower than the rated voltage of the capacitor $u_{C_{Rated}}$ divided by the charging current. Therefore, the voltage derivative of the SCM is positive when the parallel resistance is disconnected, i.e. the switch in series is open and d_k is equal to 0. However, when the switch is close and d_k is equal to 1, the derivative change of sign [10].

$$\frac{du_{C_k}}{dt} = \left(I_{Charge} - d_k \frac{u_{C_k}}{R_k}\right) \frac{1}{C} \frac{R_k}{R_k + d_k ESR_k} \tag{11}$$

$$R_k < \frac{u_{C_{Rated}}}{I_{Charge}} \tag{12}$$

Whenever a SCM reaches its target charging voltage, the parallel resistance is connected to discharge the module, avoiding the overvoltage. Afterwards, the resistance is disconnected and connected within a hysteresis band to keep the voltage close to the target one until all the SCMs in series reach the required voltage [11]. The balancing system only operates during the charging process of the SCMs and not during operation.

A diagram of the topology on which all the power supplies are based is shown in Fig. 10. For the required high current levels, parallel power supplies are connected. Each of them has its own independent SCB in order to avoid circulation currents. A current-sharing control technique is employed to obtain a balanced response of each power supply [12].

Fig. 11 shows the control strategy of the power supplies. Considering a reference current for the coil I_{ref} for N H-bridges in parallel, the voltage reference of each parallel power converter V_{ref_k} depends on the current error of the specific branch $I_k - I_{ref}/N$ and the overall current error $I - I_{ref}$. This determine the number of current sensors required, one at the output of each H-bridge plus and extra one for the overall current. The obtained reference voltage from the control module is then transformed to switching signals S_k at 1 kHz for the IGBTs with unipolar Pulse Width Modulation (PWM) technique. To enhance the performance of the system, the PWM has been combined with interleaving techniques. Interleaved operation reduce the current ripple of the coil by changing the phase Φ_k of each PWM. The phase difference of each converter is determined by the number of H-bridges in parallel [13].

$$\Phi_k = (k-1)\frac{\pi}{N} \tag{13}$$

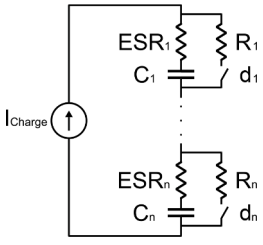

Fig. 9. Charge-balancing system.

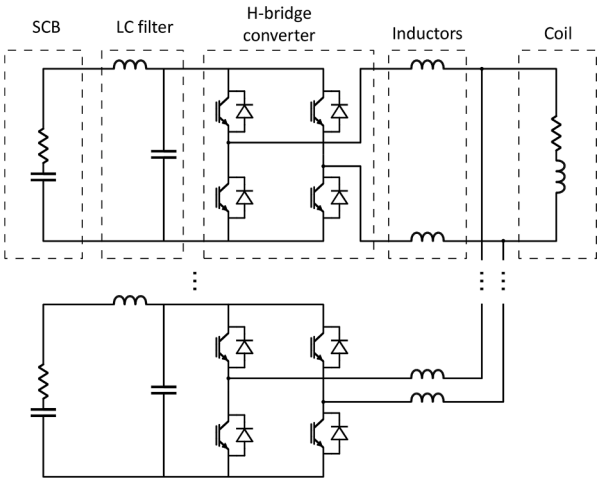

Fig. 10. Generic diagram of the power supply of a coil with the possibility of parallelization of the system.

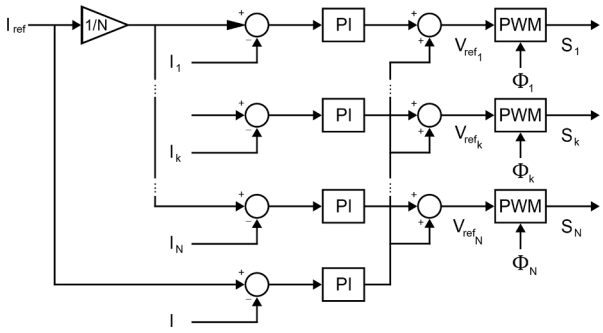

Fig. 11. Current-sharing control technique with equilibration loop.

As each power converter is working out of phase, the voltage levels at the output connections of each H-bridge can differ and decoupling inductors are required to assure safe operation [14].

CS and PFCs power supply does not required parallelization for the first operational phase of SMART. However, the high current required for TFCs makes it essential. Therefore, the power supply for the TFCs is taken as reference and explained in detail. The main parameters of the power supply are presented in Table 5. The simulated current waveform for the TFCs is shown in Fig. 12. A comparison to an arbitrary reference, reaching the operational limits of the power supply in phase 1, is also shown. The current agrees with the reference except for a ripple of 0.01 % with respect to the nominal current of 6 kA. This ripple has a

Table 5
Parameters of the TFCs power supply for phase 1.

Power supply parameters	value
Nominal current (kA)	6
No of SCB and H-bridges	4
No of SCM per SCB	6
No of current sensors	5
Parameters of each parallel branch	value
Nominal current for each branch (kA)	1.5
SCB rated voltage (V)	291.6
SCB capacitance (F)	28
SCB resistance (mΩ)	36
SCB energy (MJ)	1.2
LC filter inductance (μH)	2.7
LC filter capacitance (mF)	74
Decoupling inductance (μH)	700
Quality factor of inductances	100

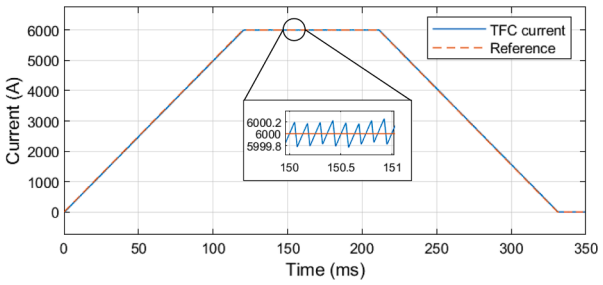

Fig. 12. TFCs current compared to reference and detail of the current ripple for the TFC power supply designed for phase 1.

frequency of 8 kHz, eight times higher than the switching frequency.The unipolar PWM doubles the resulting frequency, while the interleaving technique multiplies it by the number of converters in parallel, which in this case is 4 times.

The current ripple causes a temporal ripple in the toroidal field, in addition to the spatial ripple defined in Section 3. The definition for the spatial and temporal toroidal field ripples is the same. However, for the spatial ripple, the maximum and minimum values are for different point of the machine, while for the temporal ripple the comparison is between different moments of the same point. A finite element analysis have been employed to simulated the geometry of the vessel with its material properties to estimate the filtering effect on the magnetic fields of the eddy currents of the vacuum vessel. The result of this analysis shows that the temporal toroidal field ripple is 0.001 % inside the vessel with the same frequency than the current ripple, 8 kHz.

On the other side, a high current ripple in the SCBs causes a significant reduction of its lifetime. Therefore, a low-pass LC filter has been used to minimize it. The operation of the system without the LC filter leads to a current ripple that goes from zero to 1.5 kA with a frequency of 2 kHz, as shown in Fig. 13 for SCB1, one of the SCBs in parallel of the TFCs power supply. Furthermore, the rated voltage of the SCB1 is surpassed due to the voltage ripple. However, when the LC filter is added, the current ripple is reduced to 1.4% with respect to the 2025 kA of maximum peak current of the SCMs and Fig. 14 shows how the SCB1 operates with enough margin with respect to its maximum voltage and current limits.

For the CS and PFCs power supplies, the current ripple in the coil is always lower than 1% and in the SCBs lower than 2%.

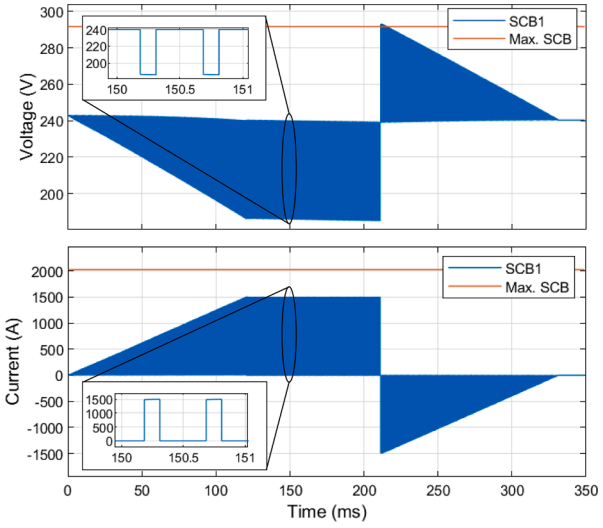

Fig. 13. Voltage and current of one TFCs SCB (SCB1) compared to their maximum rated values without the insertion of the LC filter minimizing the ripple.

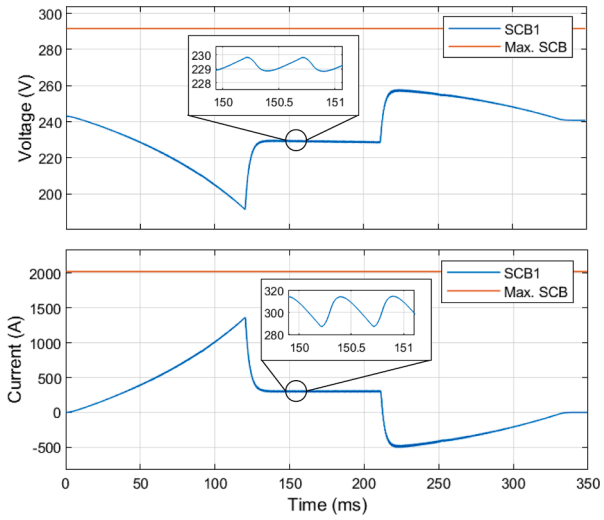

Fig. 14. Voltage and current of one TFCs SCB (SCB1) compared to their maximum rated values with the insertion of the LC filter minimizing the ripple.

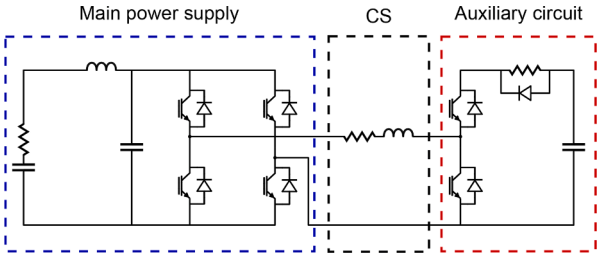

Fig. 15. CS power supply topology, including auxiliary circuit for breakdown.

In the case of the CS power supply, only one SCB and H-bridge converter is required for phase 1. However, compared to the rest of the operation, a high voltage needs to be achieved for plasma breakdown. Therefore, an auxiliary circuit, shown in Fig. 15, provides this voltage during breakdown. The auxiliary circuit have a regulated dumping resistance in parallel to a diode and in series with a capacitor of 10 mF. Its topology is equal to the one of [15]. Nevertheless, in this case the circuit is combined with a high frequency switching main power supply.

As indicated in Fig. 16, the main power supply operates for the whole CS operation, blue region, except during the greatest current slope, red region, reaching up to 350 A/ms. At this point, the main power supply is short-circuited by closing the two upper IGBTs and opening the two lower ones or vice versa. The auxiliary circuit is connected, closing the upper IGBT and opening the lower one, producing a second-order RLC dynamics that assures the required voltage and current slope for plasma breakdown. During the whole plasma breakdown, the red region, the IGBTs do not switch and the system works with an open loop control

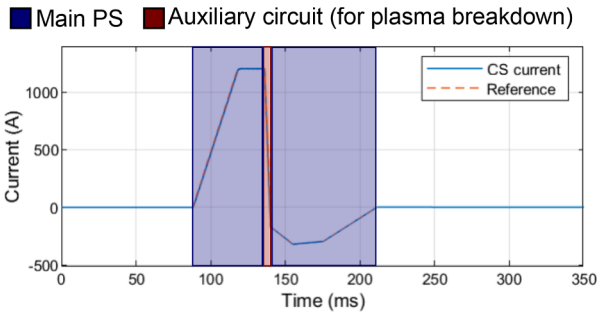

Fig. 16. CS current compared to reference, indicating when operates the main power supply or auxiliary circuit.

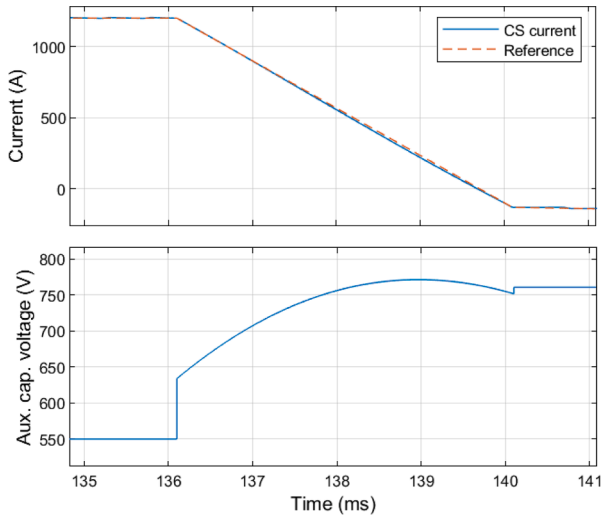

Fig. 17. Detail of the operation of the auxiliary circuit during plasma breakdown. The upper graph present the current of the CS and the lower one the voltage evolution of the auxiliary capacitor.

until the current reaches the value from which the main power supply returns to operation. Fig. 17 shows in detail the CS current waveform during this stage and how the capacitor of the auxiliary circuit is charged by the CS to obtain the desired current slope.

5. Conclusion

A system able to induce the required magnetic fields for creating and confining the plasma in SMART has been designed. The coils design maximizes the space in the central stack and is able to operate up to phase 2 with a temperature increase lower than 5 C. The power supplies are designed to provide the required current waveforms, minimizing the present and future costs. Their modular concept facilitates the upgrade for all operational phases of SMART. A preliminary analysis of the power supplies for the first phase of SMART is presented, proving their feasibility. Further work is currently under development to carry out finite element analysis to ensure the structural strength of the coils and a small-scale prototype of the power supplies is being developed as proof of concept for the present design.

Declaration of Competing Interest

The authors declare that they have no known competing financial interests or personal relationships that could have appeared to influence the work reported in this paper.

Acknowledgements

This work received funding from the Fondo Europeo de Desarollo Regional (FEDER) by the European Commission under grant agreement numbers IE17-5670 and US-15570. Furthermore, it has been carried out within the framework of the EUROfusion Consortium and has received funding from the Euratom research and training programme 2014–2018 and 2019–2020 under grant agreement no. 633053. The views and opinions expressed herein do not necessarily reflect those of the European Commission.

References

[1] Z. Gao, Compact magnetic confinement fusion: spherical torus and compact torus, Matter Radiat. Extrem. 1 (3) (2016) 153–162, https://doi.org/10.1016/j.mre.2016.05.004.
[2] K.J. Chung, Y.H. An, B.K. Jung, H.Y. Lee, C. Sung, Y.S. Na, T.S. Hahm, Y.S. Hwang, Design features and commissioning of the versatile experiment spherical torus (VEST) at Seoul National University, Plasma Sci. Technol. 15 (3) (2013) 244–251, https://doi.org/10.1088/1009-0630/15/3/11.
[3] V.A. Belyakov, V.A. Korotkov, V.F. Soikin, Design and assembly of the globus-m tokamak magnets, Plasma Devices Oper. 9 (1–2) (2001) 39–55, https://doi.org/10.1080/10519990108224486.
[4] S. Doyle, et al., Equilibrium design for the smart tokamak, Fusion Engineering and Design (submitted for publication).
[5] A. Mancini, et al., Mechanical and electromagnetic design of the vacuum vessel of the smart tokamak, Fusion Engineering and Design (submitted for publication).
[6] A. Lampasi, S. Minucci, Survey of electric power supplies used in nuclear fusion experiments. Conference Proceedings - 2017 17th IEEE International Conference on Environment and Electrical Engineering and 2017 1st IEEE Industrial and Commercial Power Systems Europe, EEEIC / I and CPS Europe 2017, Institute of Electrical and Electronics Engineers Inc., 2017, https://doi.org/10.1109/EEEIC.2017.7977851.
[7] A. Lampasi, S. Tenconi, G. Taddia, F. Gherdovich, L. Rinaldi, A new generation of power supplies for pulsed loads, Fusion Eng. Des. 146 (2019) 1921–1925, https://doi.org/10.1016/j.fusengdes.2019.03.066.
[8] IEC, Low-Voltage Electrical Installations—Part 4–43: Protection for Safety - Protection Against Overcurrent. IEC 60364-4-43:2008, International Electrotechnical Commission, 2008.
[9] P.C. De Vries, E. Joffrin, N.C. Hawkes, X. Litaudon, C.D. Challis, Y. Andrew, M. Beurskens, M. Brix, J. Brzozowski, K. Crombé, C. Giroud, J. Hobirk, T. Johnson, J. Lönnroth, A. Salmi, T. Tala, V. Yavorskij, K.D. Zastrow, Effect of toroidal field ripple on the formation of internal transport barriers, Plasma Phys. Control. Fusion 50 (6) (2008) 12, https://doi.org/10.1088/0741-3335/50/6/065008.
[10] H. Li, J. Peng, J. He, Z. Huang, J. Pan, Synchronized cell-balancing charging of supercapacitors, IFAC-PapersOnLine 50 (1) (2017) 3338–3343, https://doi.org/10.1016/j.ifacol.2017.08.518.
[11] D. Linzen, S. Buller, E. Karden, R.W. De Doncker, Analysis and evaluation of charge-balancing circuits on performance, reliability, and lifetime of supercapacitor systems, IEEE Trans. Ind. Appl. 41 (5) (2005) 1135–1141, https://doi.org/10.1109/TIA.2005.853375.
[12] M.O. Younsi, M. Bendali, T. Azib, C. Larouci, C. Marchand, G. Coquery, Current-sharing control technique of interleaved buck converter for automotive application. IET Conference Publications 2014, Institution of Engineering and Technology, 2014, https://doi.org/10.1049/cp.2014.0448.
[13] C. Boonmee, Y. Kumsuwan, A phase-shifted carrier-based PWM technique for cascaded H-bridge inverters application in standalone PV system. 15th International Power Electronics and Motion Control Conference and Exposition, EPE-PEMC 2012 ECCE Europe, 2012, https://doi.org/10.1109/EPEPEMC.2012.6397528.
[14] D. Verdugo, F. Rojas, J. Lillo, M. DIaz, J. Pereda, G. Gatica, Phase-shifted pulse width modulation with alternate zeros voltage for parallel connection of H-bridges for high-current low-voltage applications. IECON Proceedings (Industrial Electronics Conference), volume 2019-October, IEEE Computer Society, 2019, pp. 1950–1955, https://doi.org/10.1109/IECON.2019.8927568.
[15] S.C. Hong, J.Y. Park, Y.G. Kim, K.J. Chung, Y.S. Hwang, Y.S. Na, Snubber circuit optimization of the central solenoid power system for versatile experiment spherical torus. Transactions of the Korean Nuclear Society Spring Meeting, International Nuclear Information System, 2018.http://inis.iaea.org/Search/search.aspx?orig_q=RN:50059694.